

Spectral properties and modes of surface microcavities

R. C. Pennington,¹ G. D'Alessandro,² J. J. Baumberg,^{1,3} and M. Kaczmarek¹

¹*School of Physics and Astronomy, University of Southampton, Highfield, Southampton SO17 1BJ, England, United Kingdom*

²*School of Mathematics, University of Southampton, Highfield, Southampton SO17 1BJ, England, United Kingdom*

³*Cavendish Laboratory, University of Cambridge, Cambridge CB3 0HE, England, United Kingdom*

(Received 10 July 2008; revised manuscript received 6 January 2009; published 22 April 2009)

We measure experimentally the spatial intensity profiles and resonant frequencies of the transverse modes of nearly hemispherical microcavities for a range of cavity lengths and mirror curvatures. The experimental mode profiles are radially symmetric Gauss-Laguerre modes, but do not possess the radial frequency degeneracies typical of Gauss-Laguerre modes in large-scale optical cavities. We use a paraxial model of cavity propagation to interpret the experimental results. In particular, we show that the lifting of the radial frequency degeneracy may be due to the strength of spherical aberration in wavelength-scale microcavities.

DOI: [10.1103/PhysRevA.79.043822](https://doi.org/10.1103/PhysRevA.79.043822)

PACS number(s): 42.79.Gn, 42.55.Sa, 78.67.-n

I. INTRODUCTION

Wavelength-scale microcavities confine electromagnetic fields in small volumes and thus enhance light-matter interactions. This principle allows a wide range of novel devices to be developed using microcavities: ultralow threshold lasers, enhanced emitters, tunable microfilters, enhanced sensors, and resonant light-matter modulators [1–10].

Traditionally the main microcavity designs studied are pillar, planar, photonic crystal, and whispering gallery microcavities [1,2,11,12]. Pillar and planar structures are widely used to enhance the interaction of light and matter with the use of quantum dots and quantum wells [3]. Confinement in lateral directions such as photonic crystals [13,14], microcavity mesas [15], spherical microcavities, and microdisk structures [16] can inhibit spontaneous emission altogether but involve complex and generally expensive fabrication stages. Glass and polymer microspheres show high- Q factors in whispering gallery modes, but they are hard to control and it is difficult to couple light in or out [17]. Significant spontaneous emission modification and extremely low laser thresholds have been observed in spherical microcavities, similar to macroscale resonators, with two opposite mirrors [18].

Constructing cavities with the smallest possible mode volume requires mirrors with a small radius of curvature. Most of these designs are expensive and very complex to fabricate and also lack tunability in their physical dimensions. The design and fabrication of empty microcavities, which can subsequently be filled with active (in)organic materials, is also extremely difficult. While this has been achieved in planar microcavities, for instance, filled with liquid crystals to investigate tunability and optical switching [19], this has not been combined with lateral confinement.

In this paper we study experimentally and theoretically the spectral properties of nearly hemispherical microcavities consisting of a nearly hemispherical metallic mirror opposite a planar mirror [Fig. 1(a)]. These have remarkable and unique advantages with respect to the other types mentioned above: they are easy and inexpensive to fabricate, their geometrical properties can easily be changed, and they can be filled with ease with active materials. This gives them great

potential as possible liquid-crystal devices [20], atomic traps [21], and chemical and biological sensors [22,23].

Contrary to planar cavities, nearly hemispherical microcavities confine the light in the plane as well as in the vertical direction, so that the cavity modes become discrete and split into longitudinal and transverse modes. The mode structure of the microcavities can be determined analytically by solving the full Maxwell's equations with appropriate metal boundary conditions at the mirror surfaces and perfectly matched layers in the transverse plane [24,25]. Studies of pattern formation in vertical-cavity surface-emitting lasers (VCSELs) [26] of mode spectra in microdisk cavities [27] and of the ray dynamics in parabolic cavities [28] indicate that approximations normally used in macroscopic cavities are fairly accurate also in wavelength-scale cavities, but have not been applied to these new designs.

Here we use paraxial theory based on a modified Fox and Li approach [29] to study the modes of nearly hemispherical microcavities. These calculations allow us to interpret the experimental results and highlight features of the microcavities that are significantly different from macroscopic cavities: the strong circular symmetry, the large effect of the precise mirror profile on the mode structure, and the radial mode splitting induced by the nonparabolic optical elements of the microcavity. This heightened sensitivity to the geometrical optical profile of the cavity limits the ability of a paraxial theory to match exactly the experimental mode profiles. In order to do this requires devising new methods for *extremely precise* measurements of the mirror profile, which is beyond the scope of this research. This, however, should not detract from the success of the approach to understand all the salient features of the experimental spectra.

Some results of this paper have been reported earlier in [30]. Here we present and further analyze the experimental profiles and frequencies of the nearly hemispherical microcavity transverse modes for a range of different microcavity samples.

Comparing different sample geometries allows an in-depth look at how the microcavity geometry effects the experimental frequencies of the transverse modes. We have refined the gold deposition technique and are now able to control the surface roughness of the nearly hemispherical mirror. This has allowed us to measure how the roughness of the

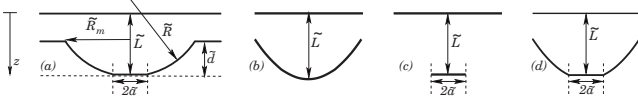


FIG. 1. Geometries of different cavity profiles: (a) soup dish, (b) parabolic, (c) aperture, and (d) parafiat. In all cavities \tilde{L} is the cavity length. (a) The soup dish cavity is closest to the experimental cavities (referred to in the text as “nearly hemispherical microcavities”). Its phase profile is given by Eq. (7). Its parameters are the radius of the sphere \tilde{R} , the radius of the flat bottom \tilde{a} , and the dish thickness \tilde{d} . (b) The parabolic cavity is a standard cavity with a parabolic mirror of radius of curvature \tilde{R} . (c) The aperture cavity has a plane mirror with aperture of radius \tilde{a} . (d) The parafiat cavity has a parabolic mirror of radius of curvature \tilde{R} and with a flat vertex of radius \tilde{a} .

optical surfaces affects the experimental frequencies of the transverse modes. We also present a perturbation expansion approach that we use to quantify the effect of spherical aberration in these cavities. Moreover, we develop a second type of perturbation expansion, this time in the cavity length, that leads to an analytical expression for the spectra and mode profiles of a model of the experimental cavity geometry.

Following this section, Sec. II presents a comprehensive description of the theoretical model. Section III describes the microcavity fabrication techniques and the experimental procedure undertaken to obtain the cavity spectra. It then goes on to discuss the observed mode intensity profiles and frequencies. Section IV presents a comparison of the predicted mode profiles and frequencies to the experimental profiles and frequencies. Section V contains the conclusions and an analysis of future developments.

II. THEORY

A. Modes of a parabolic cavity

Previous work [30] has shown that the experimental mode profiles and spectra of our nearly hemispherical microcavity structures (see Sec. III) are very reminiscent of the Gauss-Laguerre (GL) modes of macroscopic cavities in the paraxial approximation [31]. This assumes that we can represent the electromagnetic field as a light beam that propagates in a preferred direction (*longitudinal* direction) with an amplitude that is slowly varying with respect to the light wavelength. Under this approximation, the amplitude of a linearly polarized field can be written, in cylindrical coordinates (r, ϕ) , as

$$E(r, \phi, z, t) = F(r, \phi, z, t) e^{i(kz - \omega t)}, \quad (1)$$

where $k = 2\pi/\lambda$ is the light wave number, ω is the light angular frequency, z is the propagation direction, and $F(r, \phi, z, t)$ is the slowly varying amplitude. The quantities in Eq. (1) are all nondimensional: the light wavelength λ and the longitudinal coordinate z have been scaled to the length \tilde{L} of the cavity in Fig. 1. Time t has been scaled by $\tilde{\tau} = \tilde{L}/c$. The coordinates in the plane transverse to the direction of propagation (*transverse* coordinates) have been scaled by $\tilde{\ell}$

$= \sqrt{\tilde{L}\tilde{\lambda}}/\pi$ with $\tilde{\lambda}$ as the dimensional light wavelength [32]. We use the notation that all symbols with a superscript $\tilde{}$ refer to dimensional quantities with the exception of c . For example, $\tilde{\lambda}$ is dimensional, while $\lambda = \tilde{\lambda}/\tilde{L}$ is not. We have chosen to use polar coordinates (r, ϕ) in the transverse plane in view of the axial symmetry of the experimental mode profiles.

The modes of a plane parabolic cavity are Gauss-Laguerre functions identified by a longitudinal index n , a radial index p , and an azimuthal index q . Modes with the same p have the same axial symmetry. The nondimensional mode frequency, scaled to the free spectral range $\Delta\tilde{\omega}_L = \pi c/\tilde{L}$, is (see Appendix A)

$$\omega_{npq} = n + (2p + |q| + 1)\Delta\omega_T, \quad (2)$$

where $\Delta\omega_T = \pi^{-1} \arcsin(\sqrt{1/R})$ is the transverse-mode frequency spacing and R is the radius of curvature of the mirror scaled to the cavity length.

Equation (2) shows that the frequency spectrum of the modes is organized in longitudinal families, i.e., modes with the same value of n . In each family, modes with the same value of $2p + |q|$ are frequency degenerate. The $\pm q$ degeneracy is due to the axial symmetry of the cavity. It may be lifted, for example, by astigmatism. Furthermore, the degeneracy between modes that have different p and $|q|$ indices is due to presence of only parabolic elements in the cavity. This degeneracy could be lifted, for example, by spherical aberration, i.e., a quartic correction to the parabolic mirror profile. The experimental spectra shown later indicate that astigmatism is negligible in the cavity: the modes are axially symmetric and $\pm q$ degenerate. On the other hand, the degeneracy between the modes $(p, q) = (1, 0)$ and $(0, \pm 2)$ is clearly broken; therefore, we can conclude that the mirror profile cannot be considered as parabolic. A more detailed analysis of these two effects is carried out in Sec. II B.

B. Spherical aberration and astigmatism

Using scaling arguments one can give a plausible explanation of why some frequency degeneracies of the microcavity spectrum are lifted, while preserving the axial symmetry of the mode profiles. This is done by comparing the relative strength of spherical aberration and astigmatism: the former preserves axial symmetry; the latter breaks it.

In nondimensional units the phase shift induced by a spherical mirror profile of radius R is approximately

$$\delta\psi = 2r^2R^{-1} + \sigma r^4 + O(r^6). \quad (3)$$

The first term is the standard parabolic mirror profile; the second represents spherical aberration. Its strength is measured by the parameter $\sigma = k^{-1}R^{-3}$ with k as the nondimensional wave number. We note that this parameter is very small for macroscopic cavities, but *becomes significant for mirrors with radius of curvature on the order of the light wavelength*, when k becomes a quantity $O(1)$.

It is possible to compute the effect of spherical aberration on the cavity modes using a Fox and Li based treatment of the cavity modes summarized in Appendix A. The propaga-

tion in the cavity is described by a propagation operator [Eq. (A8)] that has a very simple physical meaning. The field starts at the plane mirror and propagates through free space [operator \mathcal{P}_f defined in Eq. (A7)] to the curved mirror. It is modified by the curved mirror, described by a complex function \mathcal{M} , and propagates in free space back to the plane mirror. If we represent the field as a linear combination of Gauss-Laguerre functions [Eq. (A4)] it is possible to represent the cavity propagation operator as a matrix [Eq. (A10)]. This format can then be used as the basis for a first-order perturbation expansion [33]. The mirror operator is written as the sum of an order zero parabolic profile and a first-order spherical aberration correction, i.e.,

$$\begin{aligned}\mathcal{M}(r) &= e^{i\delta\psi} \\ &= \mathcal{M}_0(r)(1 + i\sigma r^4) + O(\sigma^2) \\ &= \mathcal{M}_0(r) + \sigma\mathcal{M}_1(r) + O(\sigma^2).\end{aligned}\quad (4)$$

The order zero phase shift per round trip of the mode (p, q) is the argument of $\mu_{pq}^{(0)}$, the order zero eigenvalue. The first-order correction to this eigenvalue is

$$\mu_{pq}^{(1)} = \int_{\mathbb{R}^2} G_{pq}^*(r, \phi, -1)\mathcal{M}_1(r)G_{pq}(r, \phi, 1)rdrd\phi \quad (5)$$

and the correction to the phase shift is $\text{Im}(\mu_{pq}^{(0)*}\mu_{pq}^{(1)})$. The end result is that spherical aberration changes the frequency of the mode (p, q) by the amount

$$\Delta\Phi_{pq} = \frac{\sigma}{2\pi}C_{pq}\frac{(1+w_0^4)^2}{w_0^4}$$

with

$$C_{pq} = \frac{q^2 - 3|q| + 2}{4} + \frac{3}{2}(p+1)(p+2) + 3\left(\frac{|q|}{2} - 1\right)(p+1).$$

For example, the modes $(1,0)$ and $(0, \pm 2)$ are no longer degenerate: the modes $(0, \pm 2)$ have lower frequency and the frequency splitting is

$$\delta\epsilon_{0,\pm 2} = \frac{1}{2} \frac{\sigma}{2\pi} \frac{(1+w_0^4)^2}{w_0^4}. \quad (6)$$

This parameter is very small for macroscopic cavities, but becomes more significant for mirrors with radius of curvature on the order of the light wavelength. For the experimental-size cavities this split is equivalent to 1.5×10^{-3} , which is easily observed.

Contrary to spherical aberration, astigmatism is independent of the size of the cavity relative to the wavelength. Astigmatism can be quantified by the difference δR of the radii of curvature of the mirror in the x and y directions of an appropriate coordinate system. Therefore, the transverse-mode spacing $\Delta\omega_T = \pi^{-1} \arcsin(\sqrt{1/R})$ is different for modes aligned in the x and y directions. The frequency splitting can be obtained by expanding $\Delta\omega_T$ to first order in δR and is given by

$$-\frac{\delta R}{2\pi R\sqrt{R-1}}.$$

As expected, this is independent of the size of the cavity relative to the light wavelength. Moreover, one can reasonably assume that diffusion during the process of gold deposition will tend to reduce differences in curvature on the small scale of the experimental mirror, thus making astigmatism even more negligible with respect to scale-dependent radially symmetric effects such as spherical aberration.

C. Numerical spectra for different mirror profiles

The schematic of a typical experimental cavity is shown in Fig. 1(a). A detailed description of the system geometry and of the experimental setup is in Sec. III, but for the purpose of the analysis in this section it suffices to note that the experimental cavity has a flat mirror at the top and a curved mirror at the bottom separated by a distance \tilde{L} . The curved mirror has, in order of increasing distance from the cavity axis, a flat vertex of radius a scaled with $\tilde{\ell}$, a curved section of radius R and depth d both scaled with \tilde{L} , and then another flat part. The flat vertex is very smooth, while the curved surface and the flat boundary are rougher. It has proved an extremely difficult problem to measure the exact geometrical parameters of the cavity or, indeed, to have a completely accurate description of the cavity geometry. Similarly, we do not know yet the effect of the surface microtexture on the reflectance of the gold.

We have therefore analyzed the spectra of cavities with different mirror models: the two most significant ones from a numerical point of view are the ‘‘aperture’’ and the ‘‘soup dish’’ models, shown in Figs. 1(c) and 1(a), respectively. These have been used in Eq. (A10) to compute the modes frequencies and the spatial profiles.

In the aperture model we assume that the bottom mirror is flat and that there is a circular aperture of radius a that is perfectly absorbing. A cavity of this type is analyzed at length in [31]. The presence of the aperture gives rise to a set of discrete transverse modes. A typical set of modes is shown in Fig. 2, while the spectrum of a cavity with $\tilde{L} = 12.5 \mu\text{m}$ as a function of \tilde{a} is shown in Fig. 3. The key feature to notice in this model is that the aperture induces huge losses: the fundamental mode in Fig. 2 has loss coefficient equal to 2% per round trip, while the next mode has loss coefficient equal to 21%. We do not expect this model to be quantitatively accurate for the experimental cavity, but to display some of the qualitative features of the experimental modes (cf. Sec. III B) and of more sophisticated models (see below and Sec. II D): first, the only frequency degeneracies in the spectrum are between modes with azimuthal index $\pm q$, and second, the intermode frequency spacing decreases with the aperture radius \tilde{a} .

The other model studied numerically in some detail is the soup dish model [Fig. 1(a)]. The mirror profile in this case is $\mathcal{M}(r) = \rho(r)\exp[i2k\psi(r)]$. Here $\rho(r)$ is the loss function of the mirror: we generally assume that it is piecewise constant, with a higher value on the vertex, where the gold layer is smoother. The phase profile of the mirror is

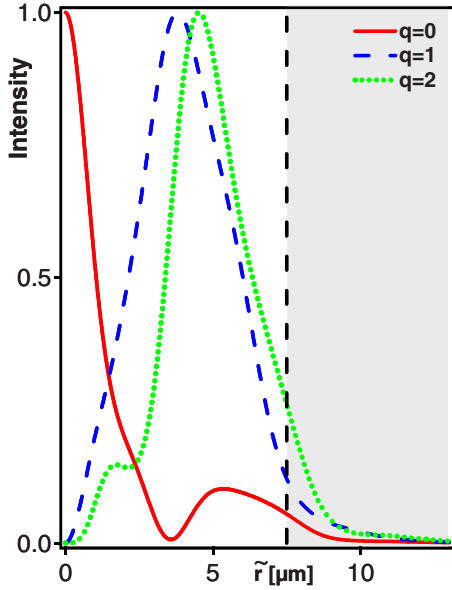


FIG. 2. (Color online) Modes of an aperture model with $\tilde{L} = 12.5 \mu\text{m}$ and $\tilde{a} = 7.5 \mu\text{m}$. The shaded region corresponds to the location of the absorbing aperture.

$$\psi(r) = \begin{cases} 0, & 0 \leq r \leq a, \\ \sqrt{R^2 - \frac{2a^2}{k}} - \sqrt{R^2 - \frac{2r^2}{k}}, & a < r \leq R_m, \\ \psi(R_m), & r > R_m, \end{cases} \quad (7)$$

where R_m is the radius of the outer rim of the curved part of the mirror scaled with $\tilde{\ell}$.

The modes of a soup dish cavity with $\tilde{L} = 12.5 \mu\text{m}$ and $\tilde{R} = 25 \mu\text{m}$ are shown in Fig. 4, while the spectrum as a function of the radius of the vertex \tilde{a} is shown in Fig. 5. As for the aperture model, the key observations are that the only degenerate modes are those with azimuthal indices $\pm q$ and that the transverse-mode spacing decreases with increasing \tilde{a} . However in this case the losses of higher-order modes are

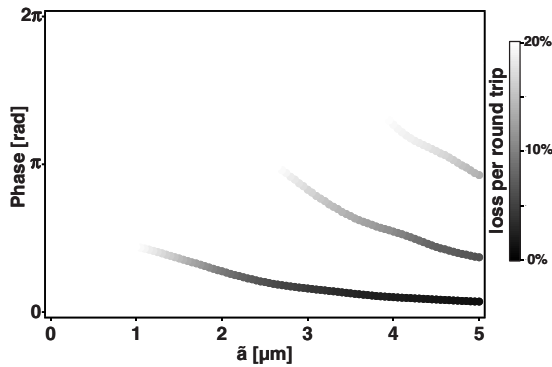


FIG. 3. Spectrum of an aperture cavity of length $\tilde{L} = 12.5 \mu\text{m}$ as function of the aperture radius. The vertical axis is the mode phase shift per round trip; the grayscale shading indicates the percentage loss per round trip. We plot only the modes with losses per round trip smaller than 20%.

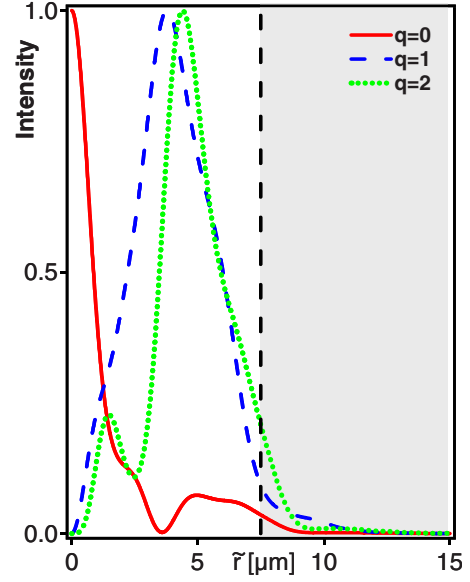


FIG. 4. (Color online) Modes of a soup dish cavity with $\tilde{L} = 12.5 \mu\text{m}$, $\tilde{a} = 7.5 \mu\text{m}$, $\tilde{R} = 25 \mu\text{m}$, and $\tilde{d} = 1.5 \mu\text{m}$. The shaded area corresponds to the curved part of the mirror [see Fig. 1(a)].

similar to those of the fundamental mode (Fig. 5). As we have assumed that the flat vertex has highest reflectance, the losses of the modes increase as they overlap more and more with the curved section of the mirror. The mode spectra of the aperture model (Fig. 3) and of the soup dish model (Fig. 5) have similar features for large a , namely, the flattening of the frequency curves of the lowest-order modes. This suggests that in both type of cavities the mode structure for large a is determined mainly by the flat part of the mirror. This is confirmed by Fig. 4 which shows that the fundamental mode is concentrated on the flat vertex of the soup dish mirror.

D. Analytical cavity models

The analysis of the numerical spectra in Sec. II C has shown that the frequencies in cavities with relative large a

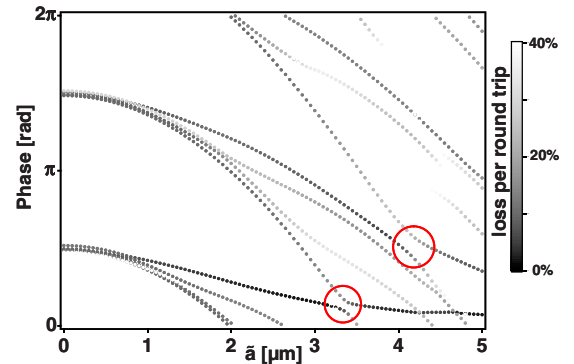


FIG. 5. (Color online) Spectrum of a soup dish cavity as a function of the radius \tilde{a} of the flat vertex. The vertical axis is the mode phase shift per round trip the grayscale shading indicates the percentage loss per round trip. We plot only the modes with loss per round trip less than 40%. The circles highlight avoided crossings in the mode spectra (see Fig. 6). Cavity parameters: $\tilde{L} = 12.5 \mu\text{m}$, $\tilde{R} = 25 \mu\text{m}$, and $\tilde{d} = 1.5 \mu\text{m}$.

are determined mainly by the flat part of the mirror. This analysis has also shown that the mode profile is quite sensitive to the cavity geometry, a phenomenon that is likely to be amplified by the presence of discontinuities in the mirror profile. To complement the numerical models detailed in Sec. II C and gain a better understanding of the microcavity spectra we have developed two closely related analytical models by considering the limiting case of cavities that are short with respect to the Rayleigh range of the modes, so that diffraction can be neglected.

We have taken a two pronged approach: we have developed a simple analytical model of an aperture cavity [Fig. 1(c)] to fit the experimental frequency spectrum. The fitted parameters can then be used in a more refined semianalytical model of a paraflat cavity [Fig. 1(d)] to obtain mode profiles that can be compared with the experimental data. The salient features of the two models can be summarized as follows.

A plane mirror cavity with circular aperture and no diffraction is equivalent to a circular waveguide with zero-field boundary conditions. The modes are Bessel functions and the frequencies are given by

$$\omega_{npq} = 2n \sqrt{1 + \frac{\rho_{pq}^2}{2n\pi a^2}}, \quad (8)$$

where ρ_{pq} is the p th zero of the Bessel function of order q and a is the radius of the aperture.

To find the mode profiles of a paraflat cavity [Fig. 1(d)] we use a perturbation expansion method based on [34]. The main idea behind this method is that the Rayleigh length of the modes is much larger than the cavity length, so that we can expand the cavity propagation operator (A8) in powers of the cavity of the length. At lowest order we find that the cavity modes obey a time-independent Schrödinger equation with the potential given by the mirror profile. The problem of finding the modes thus becomes equivalent to that of finding the eigenstates of a point particle in a cylindrical well surrounded by a radial harmonic potential. The details of the calculation are in Appendix B. The main result is that the mode profile is given by a Bessel- J function in the flat part of the mirror that is smoothly joined to a Kummer- U function [35] in the parabolic part of the mirror. We have solved the equation for the frequency of the modes in MATLAB using a custom made code to compute the Kummer- U function based in part on [35,36]. The same code can be used to plot the mode profiles that are compared to the experimental data.

A first result of this perturbation expansion approach to the study of the cavity spectra provides an insight in the structure of the mode spectrum as a function of the radius of the flat cap. Using Eqs. (B5) and (B7) it is possible to compute the frequency (or the phase shift per return trip time) of the cavity modes as a function of the radius a of the flat vertex of the mirror. A typical example is shown in Fig. 6 where the phase shifts of the modes $(p, 0)$ ($p=0, 1, \dots, 4$) are plotted as a function of \tilde{a} for a cavity with $\tilde{L}=12.5 \mu\text{m}$ and $\tilde{R}=25 \mu\text{m}$. From it we can see, first of all, that for larger values of \tilde{a} and small p the spectrum flattens, as expected for a waveguide mode. Second, at this order of the perturbation expansion there are mode crossings (highlighted by circles in

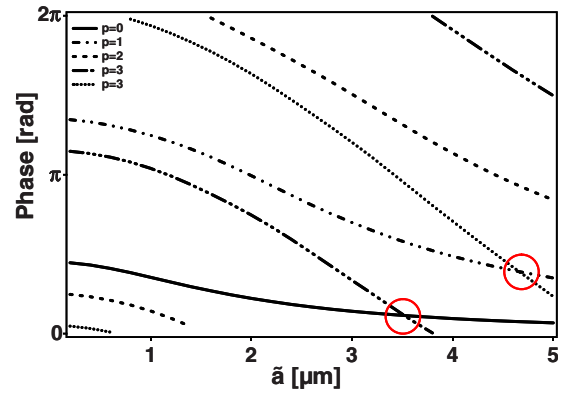


FIG. 6. (Color online) Spectrum of a paraflat mirror cavity as a function of the radius \tilde{a} of the flat vertex. The frequencies are computed to lowest order in the cavity length using Eqs. (B5) and (B7). Same cavity parameters as in Fig. 5. Note the crossings between modes (circles): these crossings are avoided in the soup dish model.

Fig. 6). This figure should be compared with the spectrum of an equivalent soup dish cavity (see Fig. 5), where some of the crossing degeneracies have been lifted. In a regular perturbation theory this eigenvalue degeneracy would be attributed to the effect of the next-order terms of the perturbation expansion. It is not possible to compute this next correction in the case of a paraflat cavity because the discontinuity of the derivative of the mirror induces singularities in the first-order corrections. However it is clear that these crossing modes mix, lifting their near degeneracy to form new superposition modes.

III. EXPERIMENT

A. Fabrication

The nearly hemispherical microcavities are fabricated by first assembling a template of latex spheres upon a gold-coated indium-tin oxide (ITO) substrate through the sedimentation of a colloidal solution. The spheres adhere to the substrate surface as the water evaporates and are left in a self-assembled arrangement. A film of gold is then electrochemically grown around them. At this stage the spheres can be dissolved away leaving spherical “dishes.” Electrochemical growth of films has a number of advantages [37]. First, it allows fine control over the thickness of the gold growth around the spheres, so that the spherical dishes have controllable height. Second, one has control over the surface roughness of the film. Also, as the spheres are dissolved there is no shrinkage of the gold growth: the resulting film is a cast of the spheres and their size controls the size of the dish. Finally, these structures are very robust and easy to fabricate.

The spherical dishes can be combined with a gold-coated planar top mirror to form microcavities of varying cavity length \tilde{L} and mirror radius \tilde{R} [38,39]. If the growth is sufficiently rapid a flat region of radius \tilde{a} is formed near the vertex of the sphere: this is used to inject light into the cavity. Figure 1(a) is a schematic drawing of the experimental cavity. In principle, all the cavity parameters and the mirror profile can be measured. However, it is nontrivial to obtain

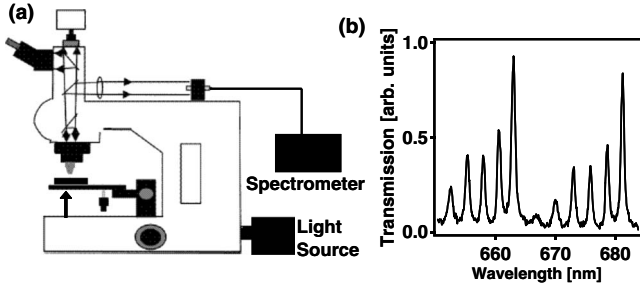


FIG. 7. (a) Experimental setup: the sample is laterally scanned using piezoelectric stage. At each position a transmission spectrum is measured using a confocally arranged fiber-coupled monochromator and cooled charge-coupled device (CCD). (b) Typical transmission spectrum, spanning two longitudinal-mode families.

accurate data, especially of the mirror profile. We have estimated the length of the cavity and the radius \tilde{a} using optical microscopy. We have assumed (based on extensive prior work [37]) that the shape of the curved mirror is a spherical ribbon of radius \tilde{R} , so that the mirror profile can be represented by Eq. (7). The use of electrochemical growth allows control of the surface roughness of the gold film, and hence the roughness of the spherical mirror. In general, the flat vertex is very smooth, while the curved surface and the flat boundary are rougher. The radius \tilde{a} of the flat bottom of the dish can also be controlled via the electrochemistry. By altering the electrochemical solution it is possible to achieve tuning between very smooth dishes (variations with respect to a smooth profile smaller than 20 nm) with very small \tilde{a} to very rough dishes (variations larger than 1 μm) with large \tilde{a} . Images of the spherical mirrors [for example, Fig. 9(i)] were taken with scanning electron microscopy (SEM) making sure that this measurement had negligible effect on the mirror surfaces. The surface roughness of the spherical mirror is quantified in terms of its topographical features. A rough

sample shows large boulderlike features of the gold growth of size larger than 1 μm . A small surface roughness mirror (smooth sample) shows no distinctive topographical features on the SEM pictures. In this case we can assume that the inhomogeneities of the gold growth are smaller than 20 nm, the resolution of the SEM.

B. Setup and experimental data

Previous work using hemispherical dishes and gold-tipped optical fibers showed that both transverse and longitudinal modes can be seen [38], but did not resolve the spatio-spectral mode structure. In order to do this we have evanescently coupled incoherent white light from a black body source through the thin gold at the base of the dish mirror. The transmission spectra are recorded on a confocally arranged fiber-coupled monochromator and cooled CCD [Fig. 7(a)]. Transmission spectra are measured as the microcavity is laterally scanned using piezoelectric stages. In this way we obtain a map of the light intensity as a function of frequency and position. A typical example of the cavity spectrum at a given position is shown in Fig. 7(b). A cross section of the map at the frequency of one of the peaks reveals the spatial structure of the corresponding cavity modes [insets (a)–(d) in Fig. 8]. Finally, we can make use of the radial symmetry of the modes to average over the angle ϕ and plot the map as a function of the radial distance \tilde{r} from the axis and the wavelength as in Fig. 8(ii). Presenting the data in this format provides a clear picture of the mode structure of the cavity.

In total 174 samples were fabricated and analyzed. The ranges of parameters for these cavities are $5.5 \leq \tilde{L} \leq 13 \mu\text{m}$ and $1.5 \leq \tilde{a} \leq 8.5 \mu\text{m}$. The radius of curvature of the mirror is either 10 or 25 μm and all samples have a dish thickness of 1.5 μm . The cavities are also differentiated by their surface roughness. The data presented here are typical of these samples. In Fig. 8 we show as an example the experimental

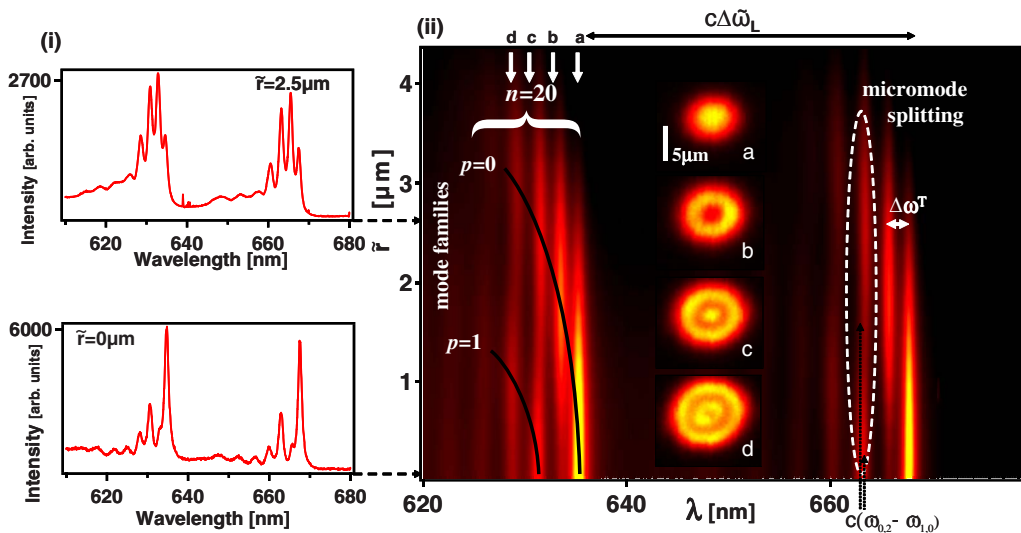


FIG. 8. (Color online) (i) Transmitted spectra at different radii from the microcavity center, $\tilde{r}=0$ and 2.5 μm , respectively. (ii) Radial intensity profiles of the transmitted light as a function of wavelength, showing families of modes with different radial indices p . Cavity parameters: $\tilde{L}=6.5 \mu\text{m}$, $\tilde{R}=10 \mu\text{m}$, $\tilde{d}=1.5 \mu\text{m}$, $\tilde{a}=3.5 \mu\text{m}$. Inset: spatial intensity distributions at wavelengths shown by arrows labeled (a)–(d).

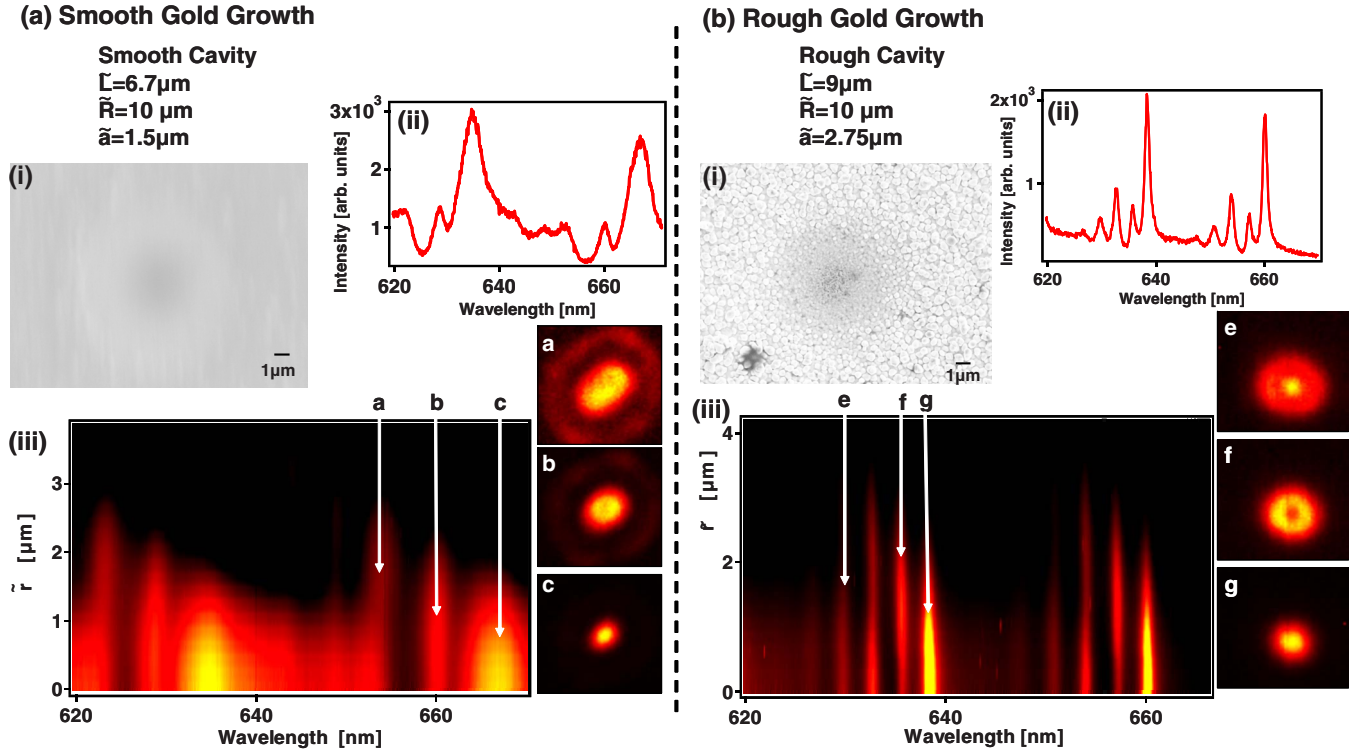


FIG. 9. (Color online) Transmission data for representative (a) smooth and (b) rough gold growth cavities, each showing (i) SEM characterization, (ii) transmission spectra measured at $\tilde{r}=0 \mu\text{m}$, and (iii) radial intensity profiles of the transmitted light as a function of wavelength. The transmission spectra are raw data and are plotted on the same scale. The relative scaling of the radial intensity profiles can be inferred from them. Insets: spatial intensity distributions at energies shown by arrows labeled as (a)–(g).

data for a cavity with $\tilde{R}=10 \mu\text{m}$, $\tilde{L}=6.5 \mu\text{m}$, and $\tilde{a}=3.5 \mu\text{m}$. All the observations that can be drawn for this cavity have been confirmed for all the other cavities.

First of all we find that the spatial intensity plots [Fig. 8 insets: spatial maps of modes for different wavelength values indicated by arrows (a)–(d)] show very clearly that the mode profiles observed are *circularly* symmetric GL modes rather than the Hermite-Gauss modes observed normally in macro-scale cavities. The slight astigmatism present in large-scale cavity is enough to split the modes into orthogonal linear families of TE_{mn} modes, but this effect is invariably completely suppressed in these micron-scale cavities.

Second, we find that there are different families of GL modes. For each longitudinal index n , two families of GL modes are seen, each with increasing azimuthal mode index, $q=0,1,2,3,4$, which form annular modes of increasing diameter. Each longitudinal family is separated by $\Delta\omega_L$, the frequency between $(p,q)=(0,0)$ of the n and $n \pm 1$ family. Surprisingly we also find that the $q>0$ modes are visible despite the fact that they are forbidden in this symmetrical coupling geometry (as the overlap integral between pump and mode is zero). We believe that the symmetry breaking which allows $q>0$ modes to be observed is produced by the surface roughness of the spherical mirror, as discussed in Sec. III C.

Third, from careful analysis of the spectra (Fig. 8) we see that the mode $(p,q)=(1,0)$ has a slightly different frequency from the modes $(p,q)=(0, \pm 2)$. This splitting is unpredicted by the paraxial theory for cavities with parabolic mirrors, as

shown by Eq. (2). Even more puzzling is the order of the modes after this splitting: $(p,q)=(1,0)$ modes have higher frequency than $(0,2)$ modes despite the fact that their energy is more concentrated toward the mirror center, where the equivalent radius of curvature is larger. This splitting and ordering of the modes is due to the nonparabolic nature of the mirror, as we have shown in Sec. II.

C. Comparison of different cavities

Smooth and rough dishes produce very different transmission data (Fig. 9). A spherical mirror which has a large surface roughness, as in Fig. 9(b), especially around the hole rim at the bottom of the spherical mirror, shows comparable transmission data to Fig. 8. The cavity modes are Gauss-Laguerre and for each longitudinal index n , two families of GL modes are seen, each with increasing azimuthal mode index, $q=0,1,2,3,4$, which form annular modes of increasing diameter. In contrast, the transmission data for a *smooth* spherical mirror [Fig. 9(a)] show that the light only couples with $q=0$ modes. The smooth gold growth seems to restrict the transverse modes. Also the $(p,q)=(0,0)$ mode is extremely broad in comparison, indicating that the cavity is lossier. Moreover, all rough samples show strong $q>0$ modes, while smooth samples have, on average, weaker coupling. This shows that the surface roughness is one source of mode-coupling factor, but there may be others. For example, the hole may not be perfectly circular or the light source not fully spatially coherent. For most cavities the strength of the

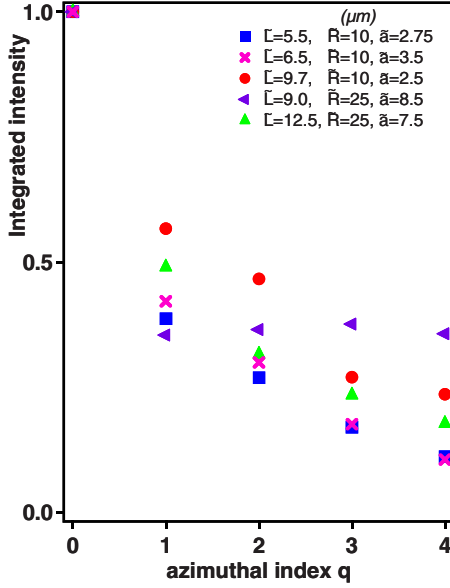


FIG. 10. (Color online) Integrated intensity normalized to that of the fundamental mode as a function of the mode number for a randomly chosen set of microcavities with large surface roughness and different values of \tilde{L} , \tilde{R} , and \tilde{a} .

higher-order modes decreases with q (see Fig. 10), as one would expect from the approximately axial symmetry of the illumination and of the cavity.

The type of experimental data presented in Fig. 8 has been taken for a range of microcavity structures each with different cavity parameters \tilde{L} , \tilde{R} , and \tilde{a} . We now explore how these parameters affect the experimental mode frequencies observed. The “transverse micromode splitting” of the azimuthal modes of fixed p , $\Delta\tilde{\omega}_q = \tilde{\omega}_{q+1} - \tilde{\omega}_q$, increases almost linearly with q and hence with the mode radius and with the overlap of the mode with the nonparabolic parts of the mirror. We find that the transverse micromode splitting is highly sensitive to the size of the flat vertex. For greater transverse micromode splitting a small \tilde{a}/\tilde{L} ratio is required. The radius of curvature \tilde{R} of the spherical mirror has little effect on the splitting, although it sets the rate of change in the splitting as the size of the hole in the bottom of the spherical mirror is increased.

According to the predictions of paraxial theory the “degeneracy splitting” $\delta\epsilon_q = \tilde{\omega}_{p+1,q-2} - \tilde{\omega}_{p,q}$ should be zero. However, the experimental modes are split by the nonparabolicity of the cavity geometry and by the wavelength scale of the cavity. Experimentally it is found that $\delta\epsilon$ increases with increasing azimuthal mode index q , most likely due to the mode experiencing more of the nonparabolic edges of the mirror. The degeneracy splitting varies slightly with the cavity parameters \tilde{L} and \tilde{a} : it increases with \tilde{L} and is inversely proportional to \tilde{a}/\tilde{L} .

To summarize, we find that the microcavity geometry has a large impact on the experimental mode frequencies observed: structures with smaller \tilde{a}/\tilde{L} have larger separation between the transverse modes and larger mode splitting; a smaller cavity length \tilde{L} produces larger longitudinal-mode

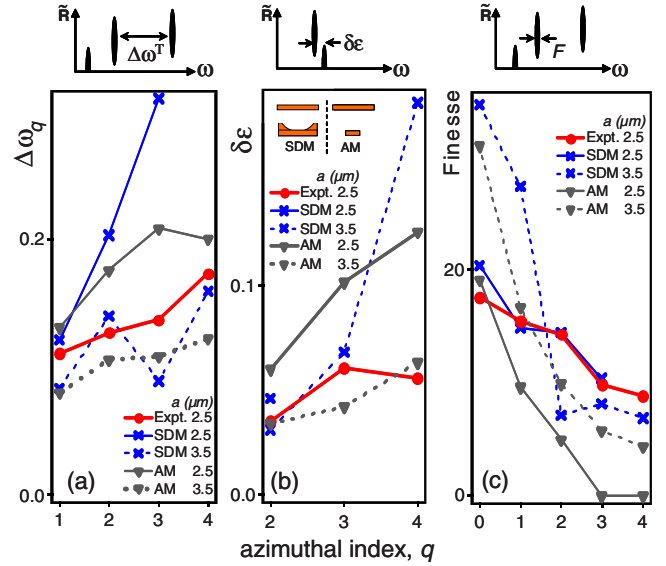


FIG. 11. (Color online) Experimental (red circles) and theoretical [soup dish model (SDM) (blue, crosses) and aperture models (AM) (black triangles) for $\tilde{a}=2.5 \mu\text{m}$ (solid lines) and $\tilde{a}=3.5 \mu\text{m}$ (dashed lines)] (a) transverse micromode splitting, (b) degeneracy lifting, and (c) finesse. $\tilde{L}=9.7 \mu\text{m}$, $\tilde{R}=10 \mu\text{m}$, and $p=0$.

separation; the radius of curvature of the spherical mirror \tilde{R} controls the scaling of longitudinal-mode separation for higher modes and also the separation between the transverse modes, but has no effect on degeneracy splitting; and the azimuthal mode index q increases the mode splittings and also the separation between the transverse modes, as larger modes experience more of the nonparabolic edges of the mirror.

IV. COMPARISON OF THEORETICAL AND EXPERIMENTAL DATA

To compare the theoretical predictions with the experimental frequencies we again look at the extracted transverse micromode splitting and degeneracy splitting. We have chosen to compare the soup dish model, as this appears to match closely the cavity geometry, and to compare it to the aperture model as this will demonstrate if, and how, the curved sides of the mirror affect the cavity modes. Both types of cavities display the qualitative features of the experimental modes and we can extract the transverse micromode splitting and degeneracy splitting from the numerical simulations. The numerical modes calculated cannot be easily indexed by (p, q) : they are just the eigenmodes of the cavity propagator given in Eq. (A10) and are not constrained to have the radial structure of the Gauss-Laguerre modes. However it is usually possible to associate indices (p, q) to the modes with lowest losses. This is what is done here when comparing numerical and experimental modes.

First, we consider the transverse micromode splitting $\Delta\omega_q$ [Fig. 11(a)]. The numerical curves for both the aperture and soup dish model show the same trend as the experimental

curves, i.e., the splitting increases almost linearly with the azimuthal index q and this behavior is highly sensitive to the size of the flat vertex \tilde{a} [Fig. 11(a)]. An approximate quantitative agreement is obtained only by using a value of \tilde{a} that is larger than the experimental \tilde{a} value.

Second, we consider the degeneracy splitting $\delta\epsilon_q$ extracted for both experiment and theory. Again the numerical curves for both the aperture and soup dish model show the same trend as the experimental curves, i.e., the splitting increases with the azimuthal index q [Fig. 11(b)], and neither of the models show a perfect quantitative agreement to the experiment at similar \tilde{a} .

There is basic agreement between both theory models and experiment which confirms that the paraxial theory is able to model the experimental cavity modes. To distinguish between these theoretical models we consider the losses of each q mode and compare with the experimental losses.

Experimentally the finesse decreases with increasing azimuthal index q , although this decrease is rather small [Fig. 11(c)] and almost linear. The higher q modes overlap more with the curved parts of the spherical mirror: these have greater surface roughness and hence are expected to induce larger losses. This behavior is consistent and reproducible over a range of microcavities. The finesse of the modes of the aperture models decreases extremely rapidly with q . It is, instead, possible to adjust the reflectance of the various parts of the soup dish mirror to obtain rates of decrease that are similar to the experimental losses. For example, in the case in Fig. 11(c) the reflectance of the soup dish mirror is set to 90% everywhere.

Finally, the radial peak positions of the $q=0$ and $q=1$ modes are compared with the experiment using the fitting procedure outlined in Sec. II D. We do not compare directly the soup dish modes because the discontinuity of the soup dish phase profile induces jagged edges in the mode profile (Fig. 4). We have measured the percentage difference of the radial peak position of the $q=1$ modes and of the full width at half maximum (FWHM) of the $q=0$ modes. They range from 3% to 62%, and the bulk of them is in the 40–50% region. Figure 12 shows the best match we have found: in this case the percentage difference of the peak positions of the $q=1$ modes is only 3%. As a rule of thumb, we have found that we can either fit the spectrum, but then predict broader modes than those experimentally observed, or fit the mode width, at the cost of having a larger transverse-mode frequency spacing than measured.

All these comparisons indicate that while our paraxial models of cavity propagation show qualitative agreement between theory and experiment, they do not produce a well-matched quantitative agreement. We expect that this is due to current limitations in determining precisely the cavity geometry coupled to the extreme sensitivity of the wavelength-scale cavities to the shape of the mirror.

V. CONCLUSIONS

In conclusion, we have successfully measured the transverse modes of a range of nearly hemispherical microcavities. In all cavities, we have observed axially symmetric

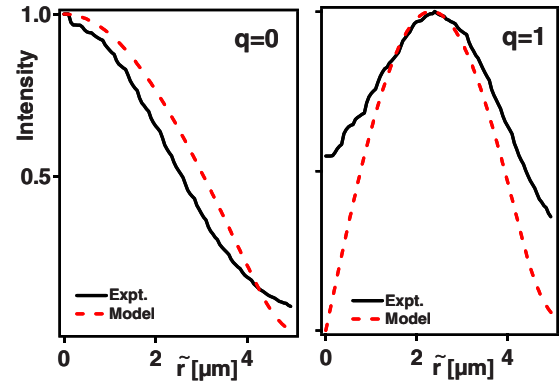


FIG. 12. (Color online) Experimental intensity profiles of the (0,0) and the (0,1) modes compared with the modes of a parafat cavity [Fig. 1(d)] whose parameters were fitted using the procedure outlined in Sec. II D. The mode profiles are given by Eqs. (B4) and (B6). The experimental and theoretical modes are scaled so the peak intensity value is equal to 1. Cavity parameters: $\tilde{L}=7.8 \mu\text{m}$, $\tilde{a}=2.25 \mu\text{m}$, and $\tilde{R}=10 \mu\text{m}$.

Gauss-Laguerre modes, with angular index $q \geq 0$. The coupling of the radially symmetric pump to modes with $q \neq 0$ is likely to be due to the mirror surface roughness. The main effect of the wavelength scale of the cavity is to amplify spherical aberration with respect to astigmatism: the frequency degeneracy between modes with different radial indices is broken, but not that between modes with opposite values of the azimuthal index. These results have been confirmed by both theory and experiment.

Comparison of the theoretical predictions with the measured experimental mode frequencies shows qualitative agreement and demonstrates that the paraxial theory is able to model the cavity modes. However, the details of the spectrum and mode profiles are highly sensitive to the cavity geometry. More accurate and advanced measurements of the experimental mirror could lead to better quantitative agreement with the theory models. However, this step is likely to be insufficient for a fully satisfactory match. Depending on the applications envisaged, one may have to revert to a full vectorial Maxwell solver, which is computationally expensive for the mode volumes discussed here. Therefore, the approach presented here offers an efficient and practical way of understanding spectral properties of microcavities with paraxial models containing all the qualitative features of the spectra.

Future work will concentrate on better controlled cavity morphologies allowing us to measure experimental spectra as a function of \tilde{a} as in Figs. 3 and 5 and to compare microcavity models and experiments. The microcavities studied here can be easily filled: the interaction between the cavity modes and the filling material is still an open question that can lead to new optical devices and sensors. For example, confining liquid crystals within the cavity leads to fast defect switching [20] that may alter the cavity spectrum in a polarization-dependent way. Filling with active nanoparticles will enable us to investigate field distributions within the cavity and study patterning instabilities within them. Coating the mirror with an electrical controllable liquid-crystal gel

will produce a surface of individually addressable electrically controlled cavities. All these developments of the basic cavities studies in this paper can be analyzed following the same principles.

ACKNOWLEDGMENTS

We acknowledge helpful discussions with Vijay Prakash and Mark Dennis and support from the EPSRC Grant No. EP/C511786/1.

APPENDIX A: MODES OF A GENERIC CAVITY

The paraxial approximation allows us to write the equation of propagation in free space [40] of a time stationary field as

$$\frac{\partial F}{\partial z} = \frac{i}{2k} \nabla_{\perp}^2 F, \quad (\text{A1})$$

where ∇_{\perp}^2 is the Laplacian operator in the transverse coordinates only. If the optical system through which the light propagates has linear optical elements with phase and gain and loss profiles that are at most parabolic in the radial transverse coordinates, then it is possible to write the field at the output as an integral transform of the field at input. The kernel of the transform depends on the *ABCD* matrices [31] of the optical system. In particular, it is possible to show that the modes of a parabolic cavity [Fig. 1(b)] are [31,32]

$$E_{npq}(r, \phi, z) = G_{pq}(r, \phi, z) e^{i(k_n z - \omega_{npq} t)}, \quad (\text{A2})$$

where $n > 0$, $p \geq 0$, and q are three integers, $k_n = 2\pi n$ is the longitudinal wave number, and ω_{npq} is the mode nondimensional frequency scaled with the longitudinal-mode frequency spacing $\Delta\tilde{\omega}_L = \pi c / \tilde{L}$,

$$\omega_{npq} = n + (2p + |q| + 1) \Delta\omega_T. \quad (\text{A3})$$

Here $\Delta\omega_T = \pi^{-1} \arcsin(\sqrt{1/R})$ is the dimensionless transverse-mode frequency spacing and R is the radius of curvature of the mirror scaled to the cavity length. The amplitude of the mode profile is [31]

$$G_{pq}(r, \phi, z) = \frac{2}{w(z)} \sqrt{\frac{p!}{2\pi(p+q)!}} \left(\frac{\sqrt{2}r}{w(z)} \right)^{|q|} L_p^{|q|} \times \left(\frac{2r^2}{w^2(z)} \right) e^{-ir^2/q(z)} e^{iq\phi} e^{i(2p+|q|+1)[\psi(z)-\psi_0]}, \quad (\text{A4})$$

where $q(z)$ is the nondimensional beam parameter, $w(z)$ is the nondimensional beam waist, and $\psi(z)$ is the propagation phase shift. We measure the longitudinal coordinate z from the point of minimum beam waist, i.e., from the plane mirrors in Fig. 1, and set $\psi_0 = \psi(0) = 0$, so that these parameters are given by

$$\frac{1}{q} \equiv \frac{1}{R_G(z)} - \frac{i}{w^2(z)} = (iw_0^2 + z)^{-1}, \quad (\text{A5})$$

$$\psi(z) = \arctan \left[\frac{w^2(z)}{R_G(z)} \right] = \arctan \left(\frac{z}{w_0^2} \right), \quad (\text{A6})$$

where w_0 is the minimum beam waist and $R_G(z)$ is the curvature of the mode wave front. The relation between the minimum beam waist and the radius of curvature R of the parabolic mirror is given by $R = 1 + w_0^4$. Both R and R_G are scaled to the length of the cavity so this relation is independent of the size of the cavity. Note that the functions $G_{pq}(r, \phi, z)$ are also solutions of the free-space propagation (A1) with initial condition $G_{pq}(r, \phi, 0)$ at $z=0$. This is a key observation for the numerical and perturbation analysis of the modes of the experimental cavities.

Equations (A2) and (A4) illustrate the meaning of the three integer indices of the modes: n is the longitudinal-mode index and is equal to the total number of half wavelengths that fit in the cavity, p is the radial mode index and is equal to the number of zeros in the radial intensity profile of the mode, and q is the azimuthal mode index and is equal to the phase winding number. We are now in a position to introduce the formalism needed to analyze the modes of cavities with nonparabolic mirrors. For these cavities it is still possible to represent field propagation as a series of integral transforms [29,31]. Propagation through free space is given by the solution of Eq. (A1). This can be formally written as propagation operator on the space of square integrable functions in the plane, $L_2(\mathbb{R}^2)$, i.e.,

$$F(r, \phi, z) = \mathcal{P}_f(z) F(r, \phi, 0) \equiv e^{(iz/2k) \nabla_{\perp}^2} F(r, \phi, 0), \quad (\text{A7})$$

where $\mathcal{P}_f(z)$ is the free-space propagation operator over a distance z . Propagation from a thin mirror is equivalent to multiplying the field by a complex function $\mathcal{M}(r, \phi)$: its phase and modulus are the mirror profile and absorption, respectively. Therefore the propagator operator for a planar-curved mirror cavity as in Fig. 1 is given by

$$\mathcal{P}_c = \mathcal{P}_f(1) \circ \mathcal{M}(r, \phi) \circ \mathcal{P}_f(1), \quad (\text{A8})$$

where \circ indicates composition of operators and $\mathcal{P}_f(1)$ is the free-space propagation between the flat and the curved mirror. The cavity modes $A_n(r, \phi)$ with \mathbf{n} as a set of indices are the eigenmodes of \mathcal{P}_c and are the solution of

$$\mathcal{P}_c A_n(r, \phi) = \mu_n A_n(r, \phi). \quad (\text{A9})$$

Equation (A9) is in an ideal format for numerical and perturbation analyses. In both cases we consider a subspace of $L_2(\mathbb{R}^2)$ spanned by a finite set of linearly independent functions. It is most convenient to choose the functions $G_{pq}(r, \phi, 0)$ as a basis, which we indicate as $|pq\rangle$, because

$$G_{pq}(r, \phi, 1) = \mathcal{P}_f(1)|pq\rangle, \quad G_{pq}^*(r, \phi, -1) = \langle pq|\mathcal{P}_f(1),$$

where the $*$ symbol indicates complex conjugate. The matrix representation of the cavity propagator (A8) becomes

$$\langle p'q' | \mathcal{P}_c | pq \rangle = \int_{\mathbb{R}^2} G_{p'q'}^*(r, \phi, -1) \mathcal{M} G_{pq}(r, \phi, 1) r dr d\phi. \quad (\text{A10})$$

If the mirror profile is axially symmetric, $\mathcal{M}(r)$, then the integral over the angle requires $q=q'$. Each angular index can be considered separately and the matrix representation (A10) of \mathcal{P}_c is block diagonal.

The matrix representation (A10) leads to a very efficient code to compute the modes of a cavity with arbitrary mirror profile, so that the calculations can be carried out using MATLAB. As both $|pq\rangle$ and $\mathcal{M}(r)$ are known analytically, it is possible to compute the integral efficiently and accurately (we have used Simpson's method as it allows us to deal quite well with nonsmooth mirror profiles). Once the matrix is computed, we determine its eigenvalues μ and eigenvectors. The latter are the decomposition of the cavity modes on the basis $\{|pq\rangle\}$. The phase shift per round trip of each mode is the argument of the corresponding eigenvalue. The loss per round trip is given by $1-|\mu|$.

APPENDIX B: MODES OF A CAVITY WITH A PARAFLAT MIRROR

The natural scaling for propagation problems in the paraxial approximation is the one used throughout this paper. However, this approach is not useful in the case analyzed in this appendix because we want to use a quantity related to \tilde{L} as a scaling parameter. In other words, we want to consider patterns much larger than $\sqrt{\tilde{L}\lambda}$, so that the effect of diffraction on propagation is comparatively small.

We therefore take the opposite scaling. We assume that there is a scaling length \tilde{w}_0 of the transverse coordinates and scale all longitudinal lengths with its Rayleigh length $\tilde{\ell}_R = 2\tilde{k}\tilde{w}_0^2$. We introduce

$$\tilde{r} = r\tilde{w}_0, \quad \tilde{z} = \tilde{\ell}_R z, \quad (\tilde{L}, \tilde{R}) = \tilde{\ell}_R (L, R),$$

where R is the nondimensional radius of curvature of the cavity mirror.

At order zero in L the cavity mode Eq. (A9) becomes a Schrödinger equation,

$$\nabla_{\perp}^2 A_n^{(0)}(r, \phi) + [E - V(r)] A_n^{(0)}(r, \phi) = 0 \quad (\text{B1})$$

with potential $V(r) = \psi(r)/2$, where $\psi(r)$ is the phase profile of the mirror. The correction to the phase shift per round trip is $2LE$. For a parafat mirror we can write

$$A_n^{(0)}(r, \phi) = R_q(r) e^{iq\phi}, \quad q \in \mathbb{N}$$

and obtain a radial equation for $R_q(r)$,

$$r^2 R_q'' + r R_q' + (Er^2 - q^2) R_q(r) = 0, \quad r \leq a, \quad (\text{B2})$$

$$r^2 R_q'' + r R_q' + \left[Er^2 - \frac{r^2(r^2 - a^2)}{4LR} - q^2 \right] R_q(r) = 0, \quad r > a. \quad (\text{B3})$$

The solution of the first is a Bessel function,

$$R_q(r) = a_q J_q(\sqrt{Er}), \quad r \leq a, \quad (\text{B4})$$

where the coefficient a_q is determined by matching at the point $r=a$.

The second equation can be recast as a Laguerre equation [41] by introducing the variable $x = r^2(2\sqrt{LR})^{-1}$ and defining

$$\left(E + \frac{a^2}{4LR} \right) \sqrt{LR} = 2p + |q| + 1. \quad (\text{B5})$$

Note that p here is no longer an integer as in the case of Gauss-Laguerre modes and should, instead, be considered as a function of E . The only bounded solution of Eq. (B5) in a domain that does not contain the origin is

$$R_q(r) = \frac{r^{|q|} e^{-r^2/(4\sqrt{LR})}}{(2\sqrt{LR})^{|q|/2}} U\left(-p, 1 + |q|, \frac{r^2}{2\sqrt{LR}}\right), \quad (\text{B6})$$

where U is the Kummer- U function [35]. The eigenvalue E is found by requiring that the two parts of the solution join with smooth first derivative at $r=a$. This condition can be recast as the following single equation for E :

$$\begin{aligned} J_q(\sqrt{Ea}) \left[4sp(q+p)U\left(-p+1, 1+q, \frac{a^2}{2s}\right) + (4ps - a^2)U \right. \\ \left. \times \left(-p, 1+q, \frac{a^2}{2s}\right) \right] + J_{q+1}(\sqrt{Ea}) 2s\sqrt{Ea}U \\ \times \left(-p, 1+q, \frac{a^2}{2s}\right) = 0, \end{aligned} \quad (\text{B7})$$

where $s = \sqrt{LR}$.

[1] K. J. Vahala, *Nature (London)* **424**, 839 (2003).

[2] A. Kavokin, J. Baumberg, G. Malpuech, and F. P. Laussy, *Microcavities* (OUP, Oxford, 2007).

[3] F. De Martini, G. Innocenti, G. R. Jacobovitz, and P. Mataloni, *Phys. Rev. Lett.* **59**, 2955 (1987).

[4] R. G. Hulet, E. S. Hilfer, and D. Kleppner, *Phys. Rev. Lett.* **55**, 2137 (1985).

[5] D. J. Heinzen, J. J. Childs, J. E. Thomas, and M. S. Feld, *Phys. Rev. Lett.* **58**, 1320 (1987).

[6] D. J. Heinzen and M. S. Feld, *Phys. Rev. Lett.* **59**, 2623 (1987).

[7] S. E. Morin, C. C. Yu, and T. W. Mossberg, *Phys. Rev. Lett.* **73**, 1489 (1994).

[8] P. R. Rice and H. J. Carmichael, *Phys. Rev. A* **50**, 4318 (1994).

[9] L. Wang, J. K. Zhang, and A. R. Bishop, *Phys. Rev. Lett.* **74**, 4710 (1995).

[10] M. Trupke, E. A. Hinds, S. Eriksson, E. A. Curtis, Z. Moktadir,

- E. Kukhareuka, and M. Kraft, *Appl. Phys. Lett.* **87**, 211106 (2005).
- [11] G. Khitrova, H. M. Gibbs, F. Jahnke, M. Kira, and S. W. Koch, *Rev. Mod. Phys.* **71**, 1591 (1999).
- [12] H. Saito, K. Nishi, I. Ogura, S. Sugou, and Y. Sugimoto, *Appl. Phys. Lett.* **69**, 3140 (1996).
- [13] E. Yablonovitch, *Phys. Rev. Lett.* **58**, 2059 (1987).
- [14] T. Yoshie, A. Scherer, J. Hendrickson, G. Khitrova, H. M. Gibbs, G. Rupper, C. Ell, O. B. Shchekin, and D. G. Deppe, *Nature (London)* **432**, 200 (2004).
- [15] J. M. Gérard, D. Barrier, J. Y. Marzin, R. Kuszelewicz, L. Manin, E. Costard, V. Thierry-Mieg, and T. Rivera, *Appl. Phys. Lett.* **69**, 449 (1996).
- [16] E. Peter, P. Senellart, D. Martrou, A. Lemaitre, J. Hours, J. M. Gerard, and J. Bloch, *Phys. Rev. Lett.* **95**, 067401 (2005).
- [17] R. Jia, D.-S. Jiang, P.-H. Tan, and B.-Q. Sun, *Appl. Phys. Lett.* **79**, 153 (2001).
- [18] G. Cui *et al.*, *Opt. Express* **14**, 2289 (2006).
- [19] S. Hoogland, J. J. Baumberg, S. Coyle, J. Baggett, M. J. Coles, and H. F. Coles, *Phys. Rev. A* **66**, 055801 (2002).
- [20] G. Vijaya Prakash, M. Kaczmarek, A. Dyadyusha, J. J. Baumberg, and G. D'Alessandro, *Opt. Express* **13**, 2201 (2005).
- [21] T. Freearde and K. Dholakia, *Phys. Rev. A* **66**, 013413 (2002).
- [22] S. Cintra, M. E. Abdelsalam, P. N. Bartlett, J. J. Baumberg, T. A. Kelf, Y. Sugawara, and A. E. Russell, *Faraday Discuss.* **132**, 191 (2006).
- [23] N. M. Perney, J. J. Baumberg, M. E. Zoorob, M. D. B. Charlton, S. Mahnkopf, and C. M. Netti, *Opt. Express* **14**, 847 (2006); <http://www.opticsexpress.org/abstract.cfm?URI=oe-14-2-847>
- [24] D. H. Foster and J. U. Nöckel, in *Laser Resonators and Beam Control VII*, Proceedings of SPIE, edited by A. V. Kudryashov and A. H. Paxton (SPIE, Bellingham, WA, 2004), Vol. 5333, pp. 195–203.
- [25] D. H. Foster and J. U. Nöckel, *Opt. Commun.* **234**, 351 (2004).
- [26] T. Ackemann, S. Barland, J. R. Tredicce, M. Cara, S. Balle, R. Jager, M. Grabherr, M. Miller, and K. J. Ebeling, *Opt. Lett.* **25**, 814 (2000).
- [27] R. P. Wang and M.-M. Dumitrescu, *J. Appl. Phys.* **81**, 3391 (1997).
- [28] J. U. Nöckel, G. Bourdon, E. Le Ru, R. Adams, I. Robert, J.-M. Moison, and I. Abram, *Phys. Rev. E* **62**, 8677 (2000).
- [29] A. G. Fox and T. Li, *Bell Syst. Tech. J.* **40**, 453 (1961).
- [30] R. C. Pennington, G. D'Alessandro, J. J. Baumberg, and M. Kaczmarek, *Opt. Lett.* **32**, 3131 (2007).
- [31] A. E. Siegman, *Lasers* (University Science, Mill Valley, CA, 1986).
- [32] L. A. Lugiato, G.-L. Oppo, J. R. Tredicce, L. M. Narducci, and M. A. Pernigo, *J. Opt. Soc. Am. B* **7**, 1019 (1990).
- [33] L. I. Schiff, *Quantum Mechanics*, 1st ed. (McGraw-Hill, New York, 1949).
- [34] C. Paré, L. Gagnon, and P. A. Bélanger, *Phys. Rev. A* **46**, 4150 (1992).
- [35] M. Abramowitz and I. A. Stegun, *Handbook of Mathematical Functions with Formulas, Graphs, and Mathematical Tables*, 9th ed. (Dover, New York, 1964).
- [36] S. Zhang and J. Jin, *Computation of Special Functions* (Wiley-Interscience, New York, 1996).
- [37] M. Abdelsalam, P. Bartlett, J. Baumberg, and S. Coyle, *Adv. Mater. (Weinheim, Ger.)* **16**, 90 (2004).
- [38] G. Vijaya Prakash, L. Besombes, T. Kelf, J. J. Baumberg, P. N. Bartlett, and M. E. Abdelsalam, *Opt. Lett.* **29**, 1500 (2004).
- [39] P. N. Bartlett, J. J. Baumberg, S. Coyle, and M. E. Abdelsalam, *Faraday Discuss.* **125**, 117 (2004).
- [40] J. V. Moloney and A. C. Newell, *Nonlinear Optics* (Addison-Wesley, Redwood City, CA, 1991).
- [41] G. B. Arfken and H. J. Weber, *Mathematical Methods for Physicists*, 5th ed. (Academic Press, London, 2001).